Applied Energy 255 (2019) 113731

Contents lists available at ScienceDirect

Applied Energy

journal homepage: www.elsevier.com/locate/apenergy

Demonstration of a kW-scale solid oxide fuel cell-calciner for power generation and production of calcined materials

Seyed Ali Nabavi[a], María Erans[a,b], Vasilije Manović[a,*]

[a] Centre for Climate and Environmental Protection, Cranfield University, Bedford, Bedfordshire MK43 0AL, UK
[b] Faculty of Engineering, University of Nottingham, Nottingham NG7 2RD, UK

HIGHLIGHTS

- A kW-scale solid oxide fuel cell-integrated calciner was designed and constructed.
- SOFC-integrated calciner generates up to 2 kW_{el} power.
- The high-grade heat generated is sufficient for full calcination of magnesite.

GRAPHICAL ABSTRACT

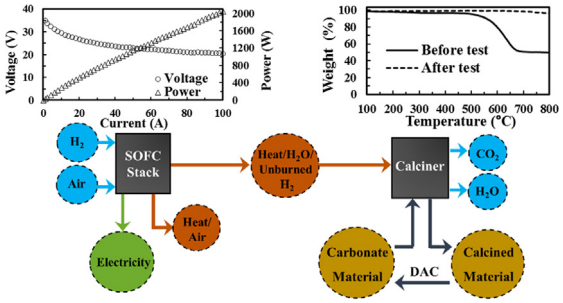

ARTICLE INFO

Keywords:
Solid oxide fuel cell
SOFC-calciner
Power generation
Calcination
Direct air capture
Negative emission

ABSTRACT

Carbonate looping (CaL) has been shown to be less energy-intensive when compared to mature carbon capture technologies. Further reduction in the efficiency penalties can be achieved by employing a more efficient source of heat for the calcination process, instead of oxy-fuel combustion. In this study, a kW-scale solid oxide fuel cell (SOFC)-integrated calciner was designed and developed to evaluate the technical feasibility of simultaneously generating power and driving the calcination process using the high-grade heat of the anode off-gas. Such a system can be integrated with CaL systems, or employed as a negative-emission technology, where the calcines are used to capture CO_2 from the atmosphere. The demonstration unit consisted of a planar SOFC stack, operating at 750 °C, and a combined afterburner/calciner to combust hydrogen slip from the anode off-gas, and thermally decompose magnesite, dolomite, and limestone. The demonstrator generated up to 2 $kW_{el,DC}$ power, achieved a temperature in the range of 530–550 °C at the inlet of the afterburner, and up to 678 °C in the calciner, which was sufficient to demonstrate full calcination of magnesite, and partial calcination of dolomite. However, in order to achieve the temperature required for calcination of limestone, further scale-up and heat integration are needed. These results confirmed technical feasibility of the SOFC-calciner concept for production of calcined materials either for the market or for direct air capture (DAC).

1. Introduction

The recent report by the Intergovernmental Panel on Climate Change (IPCC) has stressed the necessity of limiting global average warming to 1.5 °C by 2100, compared to that of the pre-industrial level, to meet global climate ambitions and minimise the severe consequences of climate change [1]. Although following the 1.5 °C emission pathway is not a geophysical impossibility yet, it requires substantial efforts to

* Corresponding author.
E-mail address: v.manovic@cranfield.ac.uk (V. Manović).

https://doi.org/10.1016/j.apenergy.2019.113731
Received 23 January 2019; Received in revised form 4 July 2019; Accepted 11 August 2019

first reduce the global net anthropogenic CO_2 emissions by almost 45% by 2030 (from 2010 levels), as the prerequisite for meeting the net zero emission around 2050 and, further to maintain negative net emissions after the mid-century [1,2].

No unique approach has been found to be solely capable of addressing the climate targets in different sectors. Although in the long-term, intermittent renewables, namely wind and solar, are regarded as the key energy technologies in the power sector, in the short-to-medium term, the utilisation of carbon capture and storage (CCS) is inevitable [3]. In addition, leading renewable technologies are associated with intermittent output, and in the absence of an efficient grid-scale energy storage technology, balancing the electricity demand and supply is challenging [4,5]. Therefore, it is more likely that a combination of renewables, nuclear, and CCS will be deployed to reduce the carbon footprint in the power sector [6]. On the other hand, in the industrial sector, energy efficiency and fuel switching have been recognised as promising pathways for the decarbonisation of energy-intensive industries [7]. However, when CO_2 is the by-product of industrial processes, it is indispensable to deploy CCS in order to mitigate the associated carbon emissions [8].

Currently, CO_2 capture technologies that exist at or near commercial scale, namely amine scrubbing and oxy-fuel combustion, are associated with high energy penalties, which make their implementation less economically viable [9]. High-temperature carbonate looping (CaL) cycles have been recognised to be promising alternatives for achieving a less energy-intensive decarbonisation solution [10,11]. CaL is based on the reversible carbonation reaction of CO_2 with metal oxides, such as calcium oxide (CaO) and magnesium oxide (MgO), at high temperatures, which is generally carried out in two interconnected circulating fluidised beds [12–14]. The carbonation takes place in the first reactor where CO_2 is captured from flue gases by the metal oxide at an elevated temperature, to form a metal carbonate. Carbonation is an exothermic process, and depending on the utilised sorbent and the feed partial pressure of CO_2, the operating temperature varies between 450 °C (magnesium-based sorbents) and 700 °C (calcium-based sorbents) [11,15]. Subsequently, the metal carbonate is transferred into the second reactor, and undergoes the calcination process at temperatures ranging from 550 °C (magnesite) to 950 °C (limestone), based on the sorbents used [11,13]. CaL has already been demonstrated in mega-watt-scale pilot plants, including the 1 MW_{th} unit in Darmstadt (Germany) [16], and the 1.7 MW_{th} unit in Oviedo (La Pereda, Spain) [17]. It is reported that the retrofit of CaL to a conventional coal-fired power plant can reduce the efficiency penalty to 5–8% [18,19], which is substantially lower than that of 9.5–12.5% for amine scrubbing [20], and 8–12% for oxy-fuel combustion [14].

The heat required to drive the calcination process is mainly provided by direct oxy-fuel combustion in the calciner in order to maintain a high-purity CO_2 stream. One of the main causes of parasitic load in CaL is attributed to the air separation unit (ASU) that supplies high-purity oxygen for oxy-fuel combustion. Thus, it is suggested that a further reduction in the efficiency penalty of the system can be potentially achieved by reducing the required amount of oxygen for the process, or eliminating the ASU. This can be accomplished by employing chemical looping [21,22], or using an alternative source of heat to drive the calcination process, including utilising heat-carrier sorbents that transfer heat from external sources [23,24], heat pipes [25,26], and heat transfer walls [27,28]. Alternatively, Ziock and Harrison [29] proposed that solid oxide fuel cells (SOFCs) could potentially be used to simultaneously generate electricity, and the high-grade heat required for the calcination process. In addition to the available high-grade heat, the anode off-gas of SOFCs (after combustion of tail gas) comprises mainly steam and CO_2 if the fuel contains hydrocarbons, that can be directly used to drive calcination and produce a pure CO_2 stream, once steam is condensed [30].

On the other hand, the SOFC-integrated calcination process can also be regarded as a negative-emission technology (NET), if the calcined materials can be used for direct air capture (DAC), in a relevant time frame. It has recently been demonstrated that dry and hydrated lime can achieve a high level of carbonation (70–75%) in a time-scale of weeks, when exposed to ambient air [31]. This time-scale is attractive from an engineering perspective, particularly when compared with the leading NETs such as bioenergy with CCS (BECCS) [32,33], and afforestation [34,35]. Hanak et al. [36] performed a techno-economic analysis on a 25 $MW_{el,DC}$ SOFC-integrated calciner for simultaneous electricity generation and DAC using limestone, dolomite, and magnesite. The system was estimated to operate at a net thermal efficiency of 43.7 (magnesite) − 47.7%$_{LHV}$ (limestone), and achieved a levelised cost of electricity of 50 £/MW_{el}h, which is competitive with other low-carbon power generation technologies. Moreover, Hanak and Manovic [37] demonstrated the feasibility of such a system under uncertainties in market conditions, where there is no economic incentive for DAC, and the system can be used to produce lime to be sold in the market. Techno-economic analyses have indicated the SOFC-integrated calciner is a promising and efficient decarbonisation concept; however, there is need to further develop and demonstrate such systems.

In this study a kW-scale SOFC-integrated calciner was designed and demonstrated, and the technical and operational challenges were evaluated. The demonstrator was used to calcine a series of carbonates, including limestone, magnesite, and dolomite. The extent of calcination was assessed using thermogravimetric analysis (TGA). The morphological variations and surface elemental analysis were characterised using scanning electron microscopy (SEM) with an energy dispersive X-ray (EDX) spectrometer. The SOFC-integrated calciner can be simply integrated with the CaL process to further reduce the energy penalty of the system, or utilised as a combined heat and power system to generate electricity and produce metal oxide, such as lime and magnesia, to be sold in the market, or used in a DAC application (NET mode).

2. Concept description

A conceptual schematic of the SOFC-integrated calcination process is presented in Fig. 1. The system comprises three main components,

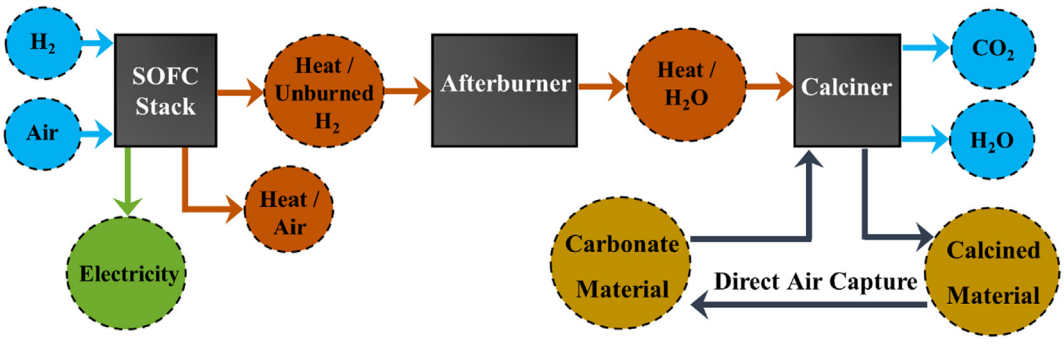

Fig. 1. Conceptual schematic representation of SOFC-integrated calcination process with CO_2 removal from the air (DAC), using carbonate materials.

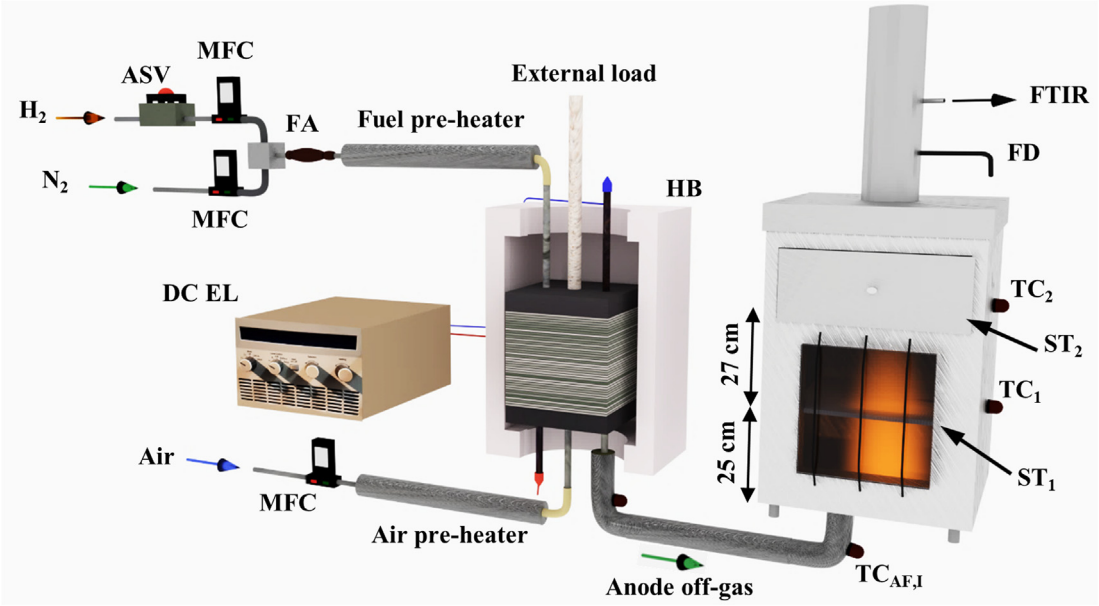

Fig. 2. Schematic of the experimental setup for demonstration of SOFC-integrated calciner. ASV is automatic shut-off valve, MFC is mass flow controller, FA is flame arrestor, ST_i is the sample tray, DC EL is direct current electronic load, HB is hotbox, FD is flue damper, TC_i is thermocouple, FTIR is Fourier-transform infrared spectroscopy.

namely SOFC stack, afterburner, and calciner. The main principle of the process is to use a SOFC stack to generate electricity, and high-grade heat to drive the calcination process. Although SOFCs can be directly fed with hydrogen and/or carbon monoxide, they are also capable of internal reforming when fed by natural gas or syngas [38]. However, internal reforming of hydrocarbons may result in carbon deposition and coke formation [39], which can cover the active side of the anode and block the microchannels [40]. To avoid coke formation within SOFCs, the reforming process can be performed externally. In general, external reforming is utilised for large-scale stationary applications, while internal reforming is employed for small-scale and portable applications to reduce the size and minimise the complexity of the systems [41]. It is recommended by the supplier (Ningbo SOFCMAN, China) that the stack used in this study needs to be operated with external reforming. Apart from mitigating carbon deposition, this also helps in avoiding feeding large amounts of steam into the stack, and increases the hydrogen partial pressure at the anode inlet to achieve a higher cell voltage [42].

When reformed gas is fed into the stack, the reformate products of methane (carbon monoxide and hydrogen), can be electrochemically oxidised on the anode side and generate electricity. However, the rate of electrochemical oxidation of carbon monoxide is 2–5 times lower than that of hydrogen. Thus, carbon monoxide mainly reacts with steam, produced due to oxidation of hydrogen or present in the feed stream, to form carbon dioxide and hydrogen through the water gas shift reaction ($CO + H_2O \rightleftharpoons CO_2 + H_2$), and the electrochemical oxidation of carbon monoxide is negligible [43]. Therefore, since the primary aim of this work was to demonstrate the feasibility of electricity generation and high-grade heat utilisation for calcination processes, and also to avoid promoting carbon deposition and complexity of the experimental rig, no external reformer was used and the stack was directly fed with hydrogen.

SOFCs typically operate at 600–1000 °C [44]. It is, therefore, expected that both anode and cathode off-gases leaving the stack are in the same temperature range. At commercial scale, the high-grade heat of the calciner and cathode off-gas can be used to preheat the air and fuel streams before feeding to the stack, as was demonstrated in our previous techno-economic studies [36,37]. However, in this demonstrator, the calciner off-gas was not utilised due to the design complexity of heat recovery at relatively small scales, i.e., relatively low flow-rates. In addition, in the SOFC stack used in this study, cathode off-gas is released from the side of the stack into the hot-box (and subsequently into the atmosphere); thus, this heat could not be utilised, Fig. S1 (Supplementary Information). Therefore, preheating of gas streams was performed using heating tapes. With regard to the anode off-gas, if the heat loss between the stack and afterburner is minimised, this stream could potentially experience a temperature rise upon combustion of the unused hydrogen, prior to the calciner.

After completion of the calcination processes, the calcined materials can be potentially transferred to a carbonator for decarbonation of flue gases (CaL) [16], sold in the market as commodities [37], or exposed to the ambient air to re-carbonate in a DAC application (NET) [31]. In addition, the concentrated CO_2 stream can be further conditioned for storage in geological formations [45], or utilised as a commercial product [46].

3. Experimental procedure

3.1. Material

Limestone (Longcliffe Ltd., UK), magnesite (Grecian Magnesite, Greece), and dolomite (Lhoist, UK) were of industrial grade, with a particle size of 100–500 μm. Nitrogen and hydrogen were supplied by BOC (UK) with a purity of higher than 99.999%. Air was provided using an air compressor.

3.2. Experimental setup

The schematic of the SOFC-integrated calciner demonstrator is presented in Fig. 2. The SOFC stack (Ningbo SOFCMAN, China) comprised 30 planar anode-supported cells, and had a configuration of Ni-YSZ/YSZ/CGO/LSCF-CGO, Fig. S1 (Supplementary Information). The cell size was 14 × 14 cm, with an active area of 150 cm^2. A 3.5 kW furnace (Ningbo SOFCMAN, China) was used to keep the stack at the desired temperature in the initiation step. The furnace was automatically switched off during the demonstration. An external pressure load of ~11.5 N cm^{-2} was applied to the stack and maintained throughout the test to ensure the stack was sealed properly. It should be noted that temperature variation during the test can affect the load.

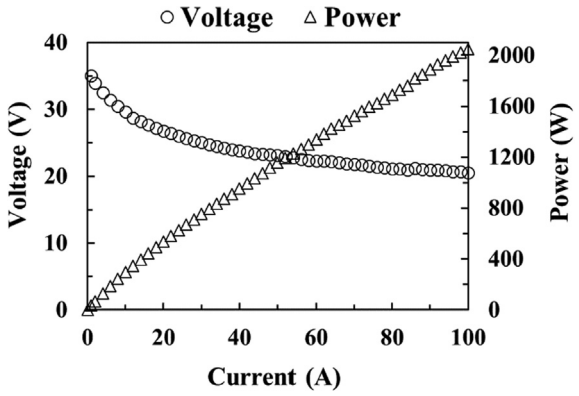

Fig. 3. Current-Voltage characteristic curves of SOFC stack at hydrogen and air flow rates of ~35 and 116 L min^{-1}, respectively.

Thus, the pressure load needed to be monitored and readjusted to 11.5 N cm^{-2}, as necessary. During operation, a DC electronic load (4.8 kW, Elektro-Automatik, Germany) was used to dissipate generated electricity. In addition, the stack voltage was measured using a multimeter (Testo, UK). 1.2 kW and 2.1 kW (0.9 kW + 1.2 kW) heating tapes (OMEGA, UK) were initially used to preheat hydrogen and air, respectively, before introduction to the stack. It should be noted that during the stable operation step, the feed gases were also heated by the exothermic reaction in the stack, which reduced the required electric power input for preheating. Thus, it is important to ensure a highly responsive temperature control system is in place to avoid overheating of the feed pipes. Prior to the installation of heating tapes, the pipe was wrapped with mica tape (COGEBI) to avoid any potential electric discharge or short circuit during operation. Moreover, to avoid any potential short circuit between the cathode and anode sides of the stack, nylon tubing was used upstream of the pre-heater in the hydrogen line to limit continuity. The flow rates of entering air, nitrogen, and hydrogen into the demonstrator were measured and controlled using mass flow controllers (Alicat, UK). The reported flow rates are based on the operating conditions of each stream. An in-house afterburner/calciner (H × W × D of 650 × 500 × 500 cm) was designed and used to burn hydrogen slip from the anode off-gas, and further calcine the carbonate materials. The furnace was constructed from polished stainless steel and lined internally with 50 mm of ridged ceramic fibre board. Considering 60–80% hydrogen utilisation within the stack, associated with a Wobbe number of ~3.4–7.8, and feed hydrogen flow rates of up to 100 L min^{-1}, a 5 kW up-fired radiant plaque burner with ceramic surface was used and situated at the base of the furnace, in order to provide an even distribution of temperature within the calciner trays. The calciner was a fixed bed, situated at the top of the furnace with the same dimensions (W × D of 500 × 500 cm), and consisted of two perforated trays located at 25 and 52 cm from the gas inlet of the burner, where the carbonate materials are placed. A flue damper (FD) was installed in the flue to adjust the amount of entering air into the afterburner. The composition of the off-gas was measured using a Fourier Transform Infrared analyser (FTIR, Protea, model FTPA-002). The safety system comprised a flame arrestor, located just before the hydrogen pre-heater, and an in-house shut-off system, including an automatic shut-off valve (ASV) in the hydrogen line, that was activated at the absence of flame in the afterburner, and/or once the temperature of the hotbox exceeded 950 °C. In addition, a hydrogen detector (Testo 316-EX, UK) was used to identify any potential leakage. The developed demonstrator rig is presented in Fig. S2 (Supplementary Information).

Prior to reducing the stack, the hotbox was preheated to 750 °C, at a rate of 1–3 °C min^{-1}. Further, the anode side was purged with 4 L min^{-1} preheated nitrogen at 600 °C for 10 min. The stack was then reduced by introducing 4 L min^{-1} preheated hydrogen at 600 °C, and 12 L min^{-1} preheated air at 500 °C into the anode and cathode sides, respectively. The reduction continued until the open circuit voltage (OCV) of the stack reached a plateau. Further, the demonstration was carried out by increasing the hydrogen and air flow rates to 18–43 L min^{-1}, and 54–150 L min^{-1}, respectively. Upon completion of the main tests, the stack was cooled to ambient temperature, at a rate of 1–2 °C min^{-1}, and under 4 L min^{-1} of hydrogen flow.

3.3. Material characterisation

3.3.1. Thermogravimetric Analysis (TGA)

The degree of calcination of the samples was measured using a thermogravimetric analyser (Pyris 1, Perkin Elmer). In each test, 20–30 mg of the material was heated from ambient temperature to 800 °C (magnesite) or 900 °C (limestone and dolomite) with a heating rate of 30 °C/min under a nitrogen flow rate of 20 mL/min, and maintained at 800 °C or 900 °C for a further 5 min.

3.3.2. Scanning Electron Microscopy – Energy Dispersive X-ray Spectroscopy (SEM-EDX)

A scanning electron microscope (FEI XL30, Philips) with an energy dispersive X-ray spectrometer (JEOL 7800F) was used to assess the morphology of the samples, and analyse the elemental compositions of their surfaces, respectively. The images were taken at an accelerated voltage of 20 keV. Prior to scanning, the samples were coated with gold nanoparticles to prevent the accumulation of electrostatic charges.

4. Results and discussion

4.1. Operating characterisation of SOFC stack

A series of experiments were designed to assess the performance of the SOFC stack with respect to power generation and operational challenges. In the first set of experiments, the reduction of the anode side was carried out at hydrogen and air flow rates of 4 and 12 L min^{-1} respectively, and continued for nearly three hours until the OCV of the stack reached a plateau of ~ 34.1 V. Further, hydrogen and air flow rates were gradually increased to nearly 35 and 116 L min^{-1}, respectively, where the performance of the SOFC stack was evaluated. Fig. 3 presents the current-voltage characteristic of the stack, measured in the constant-current mode and at a rate of ~0.6–1 A min^{-1}. At a stack current of 100 A, a stack voltage of 20.5 V was measured, indicating that the stack accomplished 2.05 kW$_{el,DC}$ (0.46 W cm^{-2} cell^{-1}) power generation. It should be highlighted that during stable operation of the demonstrator, its electric power requirement averaged 1.0 kW. Therefore, although the demonstrator generates 2 kW of electricity, the net power was reduced.

Although the local temperatures at the top and bottom of the stack were similar, ~750 °C, during the reduction process, introduction of the current load led to elevation of the local temperature at the top by ~15 °C, while no considerable change in temperature was observed at the bottom of the stack. It was also noted that an increase in hydrogen flow rates from 35 to 43 L min^{-1} further widened the top-to-bottom temperature gradient to 26 °C. However, the top-to-bottom temperature difference did not exceed the maximum threshold of 50 °C (recommended by supplier), as long as the hydrogen flow rate was kept below 43 L min^{-1}. The local temperature rise along the stack can be attributed to localised joule heating, arising from the conduction of electric current through the cell stack materials [47].

After completion of the first experiment and cooling down of the stack, it was found that a localised burn zone had formed at the front right side of the air exhaust, Fig. S3 (Supplementary Information). However, since no drop in performance of the stack was experienced during the operation, the experiment was repeated two more times to evaluate the importance of such physical damage on the effectiveness of the stack. The performance of the stack, by means of measured OCV and stack voltage, after formation of the burnt zone (first experiment) is

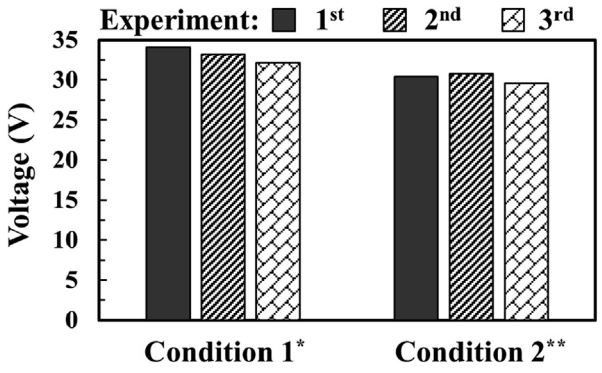

Fig. 4. Comparison of SOFC stack performance over three successive experiments and after formation of localised burnt zone. *Condition 1: Representing the stack OCV at hydrogen and air flow rates of 4 and 12 L min^{-1}, respectively. **Condition 2: Representing the stack voltage at stack current of 8 A, and hydrogen and air flow rates of ~35 and 116 L min^{-1}, respectively.

presented in Fig. 4. Condition 1 refers to comparison of OCV of the stack, measured at hydrogen and air flow rates of 4 and 12 L min^{-1}, respectively, in three successive experiments. Condition 2 refers to measured stack voltage at a stack current of 8 A, and hydrogen and air flow rates of ~35 and 116 L min^{-1}, respectively. It can be seen that there is a slight decline in the OCV of the stack (almost 2.5–3.3%) in each successive experiment. On the other hand, the stack voltage measured in a stack current of 8 A slightly increased in the second experiment, followed by a slight decrease in the third experiment. Therefore, it seems that the effect of the burnt zone on the performance of the stack at both high and low flow rates was almost negligible. However, longer experimental campaigns are needed to evaluate the effect of the burnt zone in the longer term.

It was not possible to identify at what stage (namely reduction, operation, or cool down) the burnt zone was formed. However, it can be potentially associated with localised leakage and diffusion of fuel to the cathode side which can cause the formation of localised hot spots and, eventually, partial degradation of the cells. Leakage could occur due to the presence of nucleated and propagated cracks that are formed because of residual stresses during the heating or cooling processes [48,49]. In addition, hot spots can be potentially created by localised high current-density regions due to inhomogeneous consumption of the fuel across the cell [50]. Moreover, cracks can also be caused by physical damage during the assembly, transport or installation of the stack.

4.2. Calcination of carbonates

The solid lines in Fig. 5 present the thermogravimetric analysis of carbonates, including magnesite, dolomite, and limestone under nitrogen flow, indicating the range of required temperatures for calcination. Therefore, the afterburner/calciner was designed to provide the required temperature, assuming 60–80% fuel consumption in the stack and up to 10% excess air for combustion. In the afterburner/calciner, the carbonates could be placed in two trays located at 25 cm (ST_1) and 52 cm (ST_2) from the inlet, and their temperatures, TC_1 and TC_2, respectively, were monitored, Fig. 2. In addition, the temperature of the anode off-gas stream entering the afterburner was indicated by $TC_{AF,I}$, Fig. 2.

It was seen that, when the stack was fed with hydrogen and air flow rates of ~ 35 and 116 L min^{-1}, respectively, measured TC_1 and TC_2 were as high as 449 °C and 377 °C, respectively. This implied that neither tray had sufficient temperature for the calcination of dolomite, limestone and magnesite. In addition, $TC_{AF,I}$ was around 535 °C, which was more than 200 °C lower than the operation temperature of the stack (~750 °C). The hydrogen flow rate was then gradually increased to 42 L min^{-1} while the air flow rate was kept constant, in order to slightly increase the hydrogen slip at the anode off-gas. As a result, both TC_1 and TC_2 increased up to 542 °C and 426 °C, respectively; however, there was no considerable change in $TC_{AF,I}$ (~545 °C). This implies that, if a larger stack is used, a higher temperature in the calciner can potentially be experienced. It was noted that further increase in the hydrogen flow rate resulted in a sudden increase in the local temperature at the top of the stack. Thus, the hydrogen flow rate was kept to a maximum of 43 L min^{-1}, to limit top-to-bottom temperature gradient along the stack to below 50 °C. Further, it was noted that the oxygen concentration in the flue was high (~17%), indicating massive uptake of ambient air by the afterburner. Therefore, a flue damper was utilised to reduce the amount of air entering the afterburner. Consequently, the oxygen concentration was lowered to 12%, which led to an increase in TC_1 and TC_2 to as high as 678 °C and 464 °C, respectively. In addition, almost no change in $TC_{AF,I}$ (~530 °C) was observed. The oxygen concentration of ~12% was the lowest possible that could be achieved, and any further reduction by closing the flue damper resulted in an 'abrupt cessation of combustion'. Accordingly, 150 g of carbonates was placed in tray 1 (ST_1, Fig. 2), where the highest temperatures were experienced, to proceed with the calcination process.

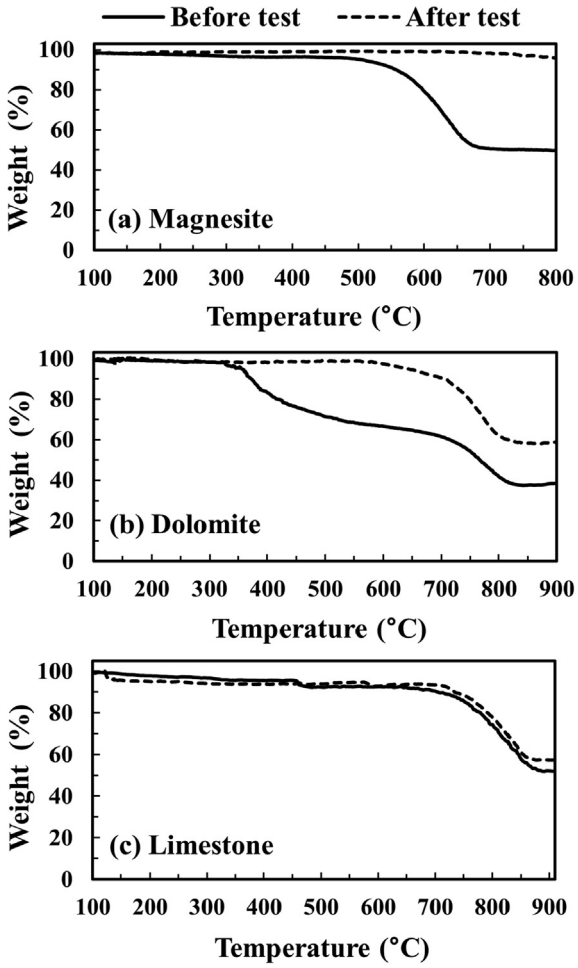

Fig. 5. TGA curves of samples before and after the test in the demonstrator, for (a) magnesite; (b) dolomite; (c) limestone.

The extent of calcination of the carbonates tested in the afterburner/calciner was assessed using TGA (Fig. 5 with the dashed lines). With regard to magnesite (Fig. 5a), no weight loss was observed in the TGA curve, implying that the sample was fully calcined in the SOFC-integrated calciner (demonstrator). This result is also confirmed by EDX analysis, Table 1, in which both magnesite samples calcined in the demonstrator and TGA had almost the same chemical composition,

Table 1
EDX elemental analysis of samples for C, O, Mg, and Ca contents (wt%).

	C	O	Mg	Ca
Magnesite	13	51	27	2
Calcined magnesite	–	38	49	1
[a]SOFC magnesite	–	37	57	1
Dolomite	6	38	10	34
Calcined dolomite	1	30	17	46
[a]SOFC dolomite	7	35	14	42
Limestone	12	40	–	48
Calcined limestone	3	22	–	74
[a]SOFC limestone	5	27	–	67

[a] SOFC magnesite/dolomite/limestone refer to samples after being tested in the demonstrator. Full EDX analyses of samples are provided in Table S1 (Supplementary Information).

with no trace of C element (presence of $MgCO_3$) in either of them. Moreover, the SEM images of both calcined magnesite samples in the TGA (Fig. 6a.2) and the demonstrator (Fig. 6a.3) appeared to be almost identical, and characterised with a less dense and more open structure compared to magnesite (Fig. 6a.1), which is attributed to the lower molar volume of MgO compared to that of $MgCO_3$.

Fig. 5b (solid line) presents the full thermal decomposition of dolomite to oxides. Although thermal decomposition of dolomite is a complex process and occurs through a series of mechanisms, overall it can be considered as a two-stage process. The first stage (here 350–700 °C) can be associated with dehydration, and decomposition of dolomite to $CaCO_3$ and MgO, while in the second stage (here 700–900 °C), $CaCO_3$ is calcined to CaO [51]. In comparison, TGA data for the dolomite sample tested in the demonstrator (Fig. 5b, dashed line) showed no significant weight loss up to ~700 °C, indicating that the demonstrator was capable of providing the temperature required to decompose dolomite to $CaCO_3$ and MgO. Further, although there was a steeper reduction in weight loss for calcined dolomite in the demonstrator (dashed line) compared to the fully calcined dolomite sample in TGA (solid line) over the temperature range of 700–750 °C, eventually both curves were almost parallel over 750–900 °C, where the calcination of $CaCO_3$ occurred. This indicates that the demonstrator was incapable of the full thermal decomposition of $CaCO_3$. In addition, EDX analysis, Table 1, showed that in comparison to dolomite, the concentration of O element of the calcined sample in the demonstrator was reduced, while the concentration of Mg and Ca increased, implying that calcination occurred to some extent. Moreover, the SEM image of the dolomite fully decomposed in the TGA, featured (Fig. 6b.2) low crystallinity which can be associated with decomposition of dolomitic calcite. On the other hand, the thermally decomposed dolomite in the demonstrator (Fig. 6b.3) showed a different structure, characterised by an amorphous phase, which may be related to poorly crystallised calcite formed due to immediate carbonation of nascent CaO crystals [52], and small MgO grains grown outwards and at the surface of the dolomite phase [53].

The calcination extent of limestone is presented in Fig. 5c. It can be seen that the TGA data for limestone sample tested in the demonstrator (dashed line) are very similar to those of fully calcined sample (solid line), with only ~11% difference in weight loss at 900 °C. This implies that calcination of limestone in the demonstrator was very limited. On the other hand, although it was expected that the EDX analysis of limestone tested in the demonstrator would be more similar to the limestone chemical composition, instead, it was found that there was more similarity to the fully calcined limestone. Moreover, comparing the SEM images of limestone (Fig. 6c.1) and fully calcined limestone (Fig. 6c.2), with the limestone sample tested in the demonstrator (Fig. 6c.3), it can be seen that there are some small CaO grains around unreacted $CaCO_3$ grains, which may relate to the occurrence of limestone calcination at low temperatures, but with slow kinetics [54]. In

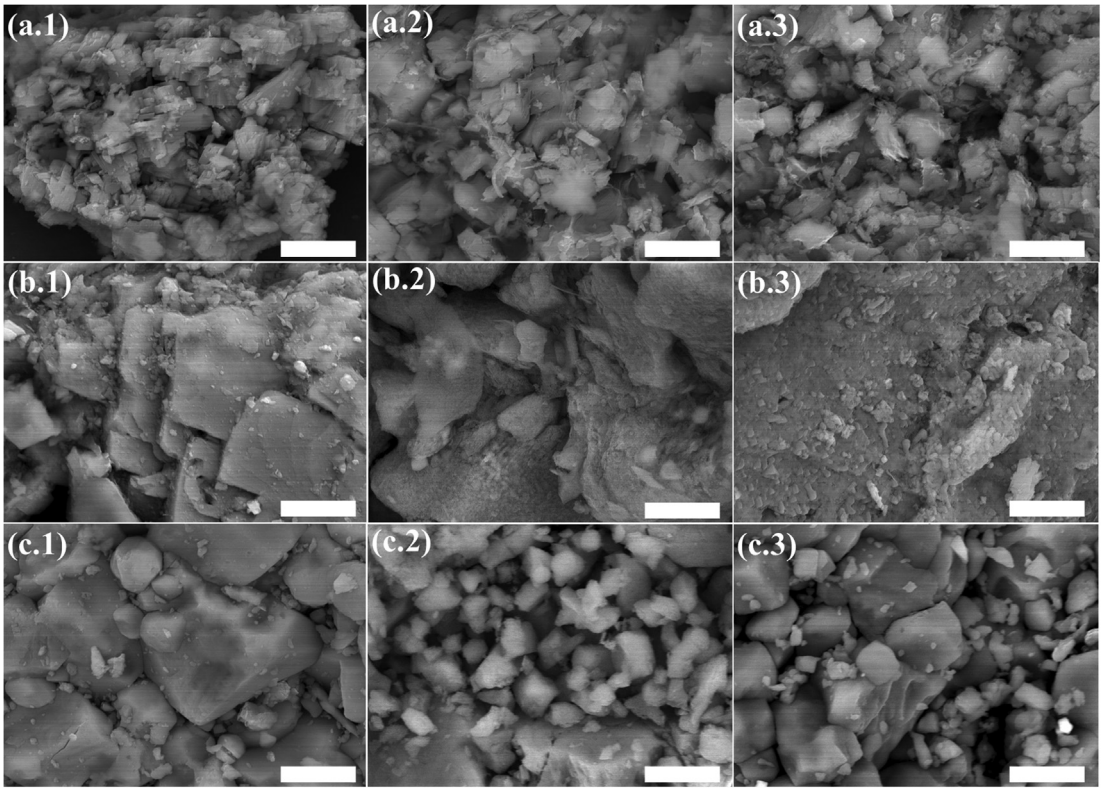

Fig. 6. SEM images of (a.1) magnesite before test; (a.2) fully calcined magnesite using TGA; (a.3) magnesite after test in SOFC-integrated calciner; (b.1) dolomite before test; (b.2) fully calcined dolomite using TGA; (b.3) dolomite after test in SOFC-integrated calciner; (c.1) limestone before test; (c.2) fully calcined limestone using TGA; (c.3) limestone after test in SOFC-integrated calciner. All scale bars are 5 μm.

addition, the smaller grain size of CaO produced in the demonstrator compared to that of the fully calcined sample is attributed to thermal decomposition at lower temperature [55].

The developed SOFC-integrated calciner demonstrated the technical feasibility of full and partial calcination of magnesite and dolomite, respectively. However, due to its relatively low cost, marked demand for lime, and the utilisation in carbonate looping cycles, calcination of limestone is still more attractive. Therefore, further improvements are needed to ensure the required temperature for the calcination of limestone in the calciner can be achieved (starting from ~840 °C for steam-rich streams [30]). The first improvement may be achieved by increasing the anode off-gas temperature entering the afterburner. As was noted, although the operating temperature of the stack was ~750 °C (recommended by supplier), the anode off-gas temperature at the inlet of the afterburner was almost 200 °C lower, despite the connecting pipe being well-insulated. This is mainly attributed to the heat losses at small scale, due to low flow rates. It was mentioned previously that some SOFCs can operate at up to 1000 °C [44] and, therefore, another solution can be to use a stack that can operate at higher temperature. However, this may lead to an increase in the degradation rate of stacks over the long term. In addition, scaling up the process means that larger SOFC stacks, operating at higher fuel flow rates should be utilised, which in turn would minimise the temperature difference between the stack exit and afterburner inlet. Moreover, once the system is scaled up, the feed gas stream can be preheated using recovered waste heat, which results in an increased net power being generated. The second improvement can be implemented by optimising the excess air fed to the afterburner. Therefore, the current afterburner can be replaced by an oxy-fuel boiler with flue gas recirculation to minimise the heat losses, required in order to produce concentrated CO_2 ready for compression and sequestration.

5. Conclusions

A kW-scale solid oxide fuel cell (SOFC)-integrated calciner was designed and constructed to explore the technical feasibility of simultaneous power generation and calcination of carbonates. Such a system not only can be regarded as an alternative for conventional calciners, where the required heat for the thermal decomposition of carbonates is provided by oxy-fuel combustion, but also, can be used as a negative-emission technology for electricity generation, if the produced calcined materials are utilised for direct air capture. The SOFC stack was successfully tested and generated up to 2 $kW_{el,DC}$ power. However, it was found that the temperature of the anode off-gas stream entering the afterburner/calciner was around 530–550 °C, at least 200 °C lower than the operating temperature of the stack (~750 °C). In addition, the maximum temperature achieved in the calciner, after combustion of the hydrogen slip of the anode off-gas, was up to 678 °C. Consequently, it was demonstrated that the SOFC-integrated calciner was capable of full and partial calcination of magnesite and dolomite, respectively. However, the extent of calcination of limestone was very low. Further improvement of such a system, by means of providing the temperature required for the calcination of limestone in a steam-rich stream, can be achieved with a scaled-up system, using larger SOFC stacks, operating at higher temperatures (up to 1000 °C). In addition, replacing the current air-fired afterburner with an oxy-fuel boiler with flue gas recirculation, which is required in order to produce concentrated CO_2 stream, and optimisation of oxygen excess ratio can address the heat losses experienced in the demonstrator and enable reaching the temperature needed for calcination of limestone.

Acknowledgment

This work is part of the “Balanced Energy Network” project supported by InnovateUK Integrated Supply Chains for Energy Systems Grant (InnovateUK reference: 102624). The consortium consists of ICAX Ltd., London South Bank University (United Kingdom), Terra Firma Ground Investigation Ltd., Upside Energy Ltd., Mixergy Ltd., Origen Power Ltd., and Cranfield University (United Kingdom). The authors would like to thank Dr Michal Jeremias, Mr Howard Smith, Dr Thomas Heenan, and Prof Dan Brett for their kind help and support during this work. Longcliffe Ltd., Grecian Magnesite, and Lhoist are acknowledged for the supply of Longcal limestone, magnesite, and dolomite, respectively. Data underlying this study can be accessed through the Cranfield University repository at https://doi.org/10.17862/cranfield.rd.9693305.

Appendix A. Supplementary data

Supplementary data to this article can be found online at https://doi.org/10.1016/j.apenergy.2019.113731.

References

[1] IPCC. Global warming of 1.5 °C (summary for policymakers). Switzerland; 2018.
[2] Millar RJ, Fuglestvedt JS, Friedlingstein P, Rogelj J, Grubb MJ, Matthews HD, et al. Emission budgets and pathways consistent with limiting warming to 1.5 °C. Nat Geosci 2017;10:741.
[3] Brouwer AS, van den Broek M, Zappa W, Turkenburg WC, Faaij A. Least-cost options for integrating intermittent renewables in low-carbon power systems. Appl Energy 2016;161:48–74. https://doi.org/10.1016/j.apenergy.2015.09.090.
[4] Heuberger CF, Staffell I, Shah N, Mac Dowell N. A systems approach to quantifying the value of power generation and energy storage technologies in future electricity networks. Comput Chem Eng 2017;107:247–56. https://doi.org/10.1016/j.compchemeng.2017.05.012.
[5] Heuberger CF, Staffell I, Shah N, Mac Dowell N. Quantifying the value of CCS for the future electricity system. Energy Environ Sci 2016;9:2497–510. https://doi.org/10.1039/C6EE01120A.
[6] Bui M, Adjiman CS, Bardow A, Anthony EJ, Boston A, Brown S, et al. Carbon capture and storage (CCS): the way forward. Energy Environ Sci 2018;11:1062–176. https://doi.org/10.1039/C7EE02342A.
[7] Chowdhury JI, Hu Y, Haltas I, Balta-Ozkan N, Matthew GJ, Varga L. Reducing industrial energy demand in the UK: A review of energy efficiency technologies and energy saving potential in selected sectors. Renew Sustain Energy Rev 2018;94:1153–78. https://doi.org/10.1016/j.rser.2018.06.040.
[8] Herzog H, Golomb D. Carbon capture and storage from fossil fuel use. New York (USA): Encycl. Energy; 2014. p. 277–87.
[9] Hanak DP, Biliyok C, Anthony EJ, Manovic V. Modelling and comparison of calcium looping and chemical solvent scrubbing retrofits for CO_2 capture from coal-fired power plant. Int J Greenh Gas Control 2015;42:226–36. https://doi.org/10.1016/j.ijggc.2015.08.003.
[10] Schlögl R, Abanades C, Aresta M, Azapagic A, Blekkan EA, Cantat T, et al. Novel carbon capture and utilisation technologies: research and climate aspects. Berlin (Germany): SAPEA; 2018.
[11] Hanak DP, Michalski S, Manovic V. From post-combustion carbon capture to sorption-enhanced hydrogen production: a state-of-the-art review of carbonate looping process feasibility. Energy Convers Manag 2018;177:428–52. https://doi.org/10.1016/j.enconman.2018.09.058.
[12] Shimizu T, Hirama T, Hosoda H, Kitano K, Inagaki M, Tejima K. A twin fluid-bed reactor for removal of CO_2 from combustion processes. Chem Eng Res Des 1999;77:62–8. https://doi.org/10.1205/026387699525882.
[13] Hanak DP, Erans M, Nabavi SA, Jeremias M, Romeo LM, Manovic V. Technical and economic feasibility evaluation of calcium looping with no CO_2 recirculation. Chem Eng J 2018;335:763–73. https://doi.org/10.1016/j.cej.2017.11.022.
[14] Boot-Handford ME, Abanades JC, Anthony EJ, Blunt MJ, Brandani S, Mac Dowell N, et al. Carbon capture and storage update. Energy Environ Sci 2014;7:130–89. https://doi.org/10.1039/c3ee42350f.
[15] Oates JAH. Lime and limestone: chemistry and technology, production and uses. John Wiley & Sons; 2008.
[16] Ströhle J, Junk M, Kremer J, Galloy A, Epple B. Carbonate looping experiments in a 1MWth pilot plant and model validation. Fuel 2014;127:13–22. https://doi.org/10.1016/j.fuel.2013.12.043.
[17] Arias B, Diego ME, Abanades JC, Lorenzo M, Diaz L, Martínez D, et al. Demonstration of steady state CO_2 capture in a 1.7MWth calcium looping pilot. Int J Greenh Gas Control 2013;18:237–45. https://doi.org/10.1016/j.ijggc.2013.07.014.
[18] Perejón A, Romeo LM, Lara Y, Lisbona P, Martínez A, Valverde JM. The calcium-looping technology for CO_2 capture: on the important roles of energy integration and sorbent behavior. Appl Energy 2016;162:787–807. https://doi.org/10.1016/j.apenergy.2015.10.121.
[19] Hanak DP, Anthony EJ, Manovic V. A review of developments in pilot-plant testing and modelling of calcium looping process for CO_2 capture from power generation systems. Energy Environ Sci 2015;8:2199–249. https://doi.org/10.1039/C5EE01228G.
[20] Xu G, Jin H, Yang Y, Xu Y, Lin H, Duan L. A comprehensive techno-economic analysis method for power generation systems with CO_2 capture. Int J Energy Res

2010;34:321–32. https://doi.org/10.1002/er.1559.
[21] Abanades JC, Murillo R, Fernandez JR, Grasa G, Martínez I. New CO_2 capture process for hydrogen production combining Ca and Cu chemical loops. Environ Sci Technol 2010;44:6901–4. https://doi.org/10.1021/es101707t.
[22] Manovic V, Anthony EJ. Integration of calcium and chemical looping combustion using composite CaO/CuO-based materials. Environ Sci Technol 2011;45:10750–6. https://doi.org/10.1021/es202292c.
[23] Martínez I, Murillo R, Grasa G, Rodríguez N, Abanades JC. Conceptual design of a three fluidised beds combustion system capturing CO_2 with CaO. Int J Greenh Gas Control 2011;5:498–504. https://doi.org/10.1016/j.ijggc.2010.04.017.
[24] Abanades JC, Anthony EJ, Wang J, Oakey JE. Fluidized bed combustion systems integrating CO_2 capture with CaO. Environ Sci Technol 2005;39:2861–6. https://doi.org/10.1021/es0496221.
[25] Reitz M, Junk M, Ströhle J, Epple B. Design and erection of a 300 kWth indirectly heated carbonate looping test facility. Energy Procedia 2014;63:2170–7. https://doi.org/10.1016/j.egypro.2014.11.236.
[26] Junk M, Reitz M, Ströhle J, Epple B. Thermodynamic evaluation and cold flow model testing of an indirectly heated carbonate looping process. Chem Eng Technol 2013;36:1479–87. https://doi.org/10.1002/ceat.201300019.
[27] Hanak DP, Manovic V. Calcium looping combustion for high-efficiency low-emission power generation. J Clean Prod 2017;161:245–55. https://doi.org/10.1016/j.jclepro.2017.05.080.
[28] Moon H, Yoo H, Seo H, Park Y-K, Cho HH. Thermal design of heat-exchangeable reactors using a dry-sorbent CO_2 capture multi-step process. Energy 2015;84:704–13. https://doi.org/10.1016/j.energy.2015.03.034.
[29] Ziock H-J, Lackner KS, Harrison DP. Zero emission coal power, a new concept. NM (US): Los Alamos National Lab; 2001.
[30] Erans M, Nabavi SA, Manović V. Pilot-scale calcination of limestone in steam-rich gas for direct air capture. Energy Convers Manag X 2019:100007.
[31] Erans M, Nabavi SA, Manović V. Carbonation of CaO-based materials under ambient conditions for direct air capture. J Clean Prod 2019.
[32] Fajardy M, Chiquier S, Mac Dowell N. Investigating the BECCS resource nexus: delivering sustainable negative emissions. Energy Environ Sci 2018;11:3408–30. https://doi.org/10.1039/C8EE01676C.
[33] Fajardy M, Mac Dowell N. The energy return on investment of BECCS: is BECCS a threat to energy security? Energy Environ Sci 2018;11:1581–94. https://doi.org/10.1039/C7EE03610H.
[34] Fuss S, Lamb WF, Callaghan MW, Hilaire J, Creutzig F, Amann T, et al. Negative emissions—Part 2: Costs, potentials and side effects. Environ Res Lett 2018;13:63002.
[35] van Vuuren DP, Stehfest E, Gernaat DEHJ, van den Berg M, Bijl DL, de Boer HS, et al. Alternative pathways to the 1.5 °C target reduce the need for negative emission technologies. Nat Clim Chang 2018;8:391–7. https://doi.org/10.1038/s41558-018-0119-8.
[36] Hanak DP, Jenkins BG, Kruger T, Manovic V. High-efficiency negative-carbon emission power generation from integrated solid-oxide fuel cell and calciner. Appl Energy 2017;205:1189–201. https://doi.org/10.1016/j.apenergy.2017.08.090.
[37] Hanak DP, Manovic V. Combined heat and power generation with lime production for direct air capture. Energy Convers Manag 2018;160:455–66. https://doi.org/10.1016/j.enconman.2018.01.037.
[38] Barelli L, Bidini G, Cinti G, Gallorini F, Pöniz M. SOFC stack coupled with dry reforming. Appl Energy 2017;192:498–507. https://doi.org/10.1016/j.apenergy.2016.08.167.
[39] Papurello D, Iafrate C, Lanzini A, Santarelli M. Trace compounds impact on SOFC performance: experimental and modelling approach. Appl Energy 2017;208:637–54. https://doi.org/10.1016/j.apenergy.2017.09.090.
[40] Stoeckl B, Subotić V, Preininger M, Schroettner H, Hochenauer C. SOFC operation with carbon oxides: experimental analysis of performance and degradation. Electrochim Acta 2018;275:256–64. https://doi.org/10.1016/j.electacta.2018.04.036.
[41] Cimenti M, Hill JM. Direct utilization of liquid fuels in SOFC for portable applications: challenges for the selection of alternative anodes. Energies 2009;2:377–410. https://doi.org/10.3390/en20200377.
[42] Cocco D, Tola V. Externally reformed solid oxide fuel cell–micro-gas turbine (SOFC–MGT) hybrid systems fueled by methanol and di-methyl-ether (DME). Energy 2009;34:2124–30. https://doi.org/10.1016/j.energy.2008.09.013.
[43] Chuahy FDF, Kokjohn SL. Solid oxide fuel cell and advanced combustion engine combined cycle: a pathway to 70% electrical efficiency. Appl Energy 2019;235:391–408. https://doi.org/10.1016/j.apenergy.2018.10.132.
[44] Timurkutluk B, Timurkutluk C, Mat MD, Kaplan Y. A review on cell/stack designs for high performance solid oxide fuel cells. Renew Sustain Energy Rev 2016;56:1101–21. https://doi.org/10.1016/j.rser.2015.12.034.
[45] Aminu MD, Nabavi SA, Rochelle CA, Manovic V. A review of developments in carbon dioxide storage. Appl Energy 2017;208:1389–419. https://doi.org/10.1016/j.apenergy.2017.09.015.
[46] Cuéllar-Franca RM, Azapagic A. Carbon capture, storage and utilisation technologies: A critical analysis and comparison of their life cycle environmental impacts. J CO_2 Util 2015;9:82–102. https://doi.org/10.1016/j.jcou.2014.12.001.
[47] Lu Y, Schaefer L, Li P. Numerical study of a flat-tube high power density solid oxide fuel cell: Part I. Heat/mass transfer and fluid flow. J Power Sources 2005;140:331–9. https://doi.org/10.1016/j.jpowsour.2004.08.036.
[48] Shao Q, Bouhala L, Fiorelli D, Fahs M, Younes A, Núñez P, et al. Influence of fluid flow and heat transfer on crack propagation in SOFC multi-layered like material with anisotropic porous layers. Int J Solids Struct 2016;78–79:189–98. https://doi.org/10.1016/j.ijsolstr.2015.08.026.
[49] Guk E, Kim J-S, Ranaweera M, Venkatesan V, Jackson L. In-situ monitoring of temperature distribution in operating solid oxide fuel cell cathode using proprietary sensory techniques versus commercial thermocouples. Appl Energy 2018;230:551–62. https://doi.org/10.1016/j.apenergy.2018.08.120.
[50] Schluckner C, Subotić V, Preißl S, Hochenauer C. Numerical analysis of flow configurations and electrical contact positions in SOFC single cells and their impact on local effects. Int J Hydrogen Energy 2018. https://doi.org/10.1016/j.ijhydene.2018.11.132.
[51] Olszak-Humienik M, Jablonski M. Thermal behavior of natural dolomite. J Therm Anal Calorim 2015;119:2239–48. https://doi.org/10.1007/s10973-014-4301-6.
[52] Valverde JM, Perejon A, Medina S, Perez-Maqueda LA. Thermal decomposition of dolomite under CO_2: insights from TGA and in situ XRD analysis. Phys Chem Chem Phys 2015;17:30162–76. https://doi.org/10.1039/C5CP05596B.
[53] Galai H, Pijolat M, Nahdi K, Trabelsi-Ayadi M. Mechanism of growth of MgO and $CaCO_3$ during a dolomite partial decomposition. Solid State Ionics 2007;178:1039–47. https://doi.org/10.1016/j.ssi.2007.05.013.
[54] Sakadjian BB, Iyer MV, Gupta H, Fan L-S. Kinetics and structural characterization of calcium-based sorbents calcined under subatmospheric conditions for the high-temperature CO_2 capture process. Ind Eng Chem Res 2007;46:35–42. https://doi.org/10.1021/ie060214a.
[55] Valverde JM, Sanchez-Jimenez PE, Perez-Maqueda LA. Limestone Calcination nearby equilibrium: kinetics, CaO crystal structure, sintering and reactivity. J Phys Chem C 2015;119:1623–41. https://doi.org/10.1021/jp508745u.